ACS APPLIED NANO MATERIALS

www.acsanm.org Article

Silicon Electrodes Functionalized with Perylene Bisimide π-Aggregates for Redox-Controlled Stabilization of Semiconducting Nanointerfaces

Arindam Mukhopadhyay, Kaixuan Liu, Victor Paulino, Carrie L. Donley, and Jean-Hubert Olivier*

Cite This: *ACS Appl. Nano Mater.* 2021, 4, 8813–8822 Read Online

ACCESS | Metrics & More | Article Recommendations | Supporting Information

ABSTRACT: While the functionalization of silicon electrode surfaces with molecularly dissolved chromophores paves the way to create diverse redox-responsive interfaces, leveraging nanoscale objects derived from π-conjugated organic building blocks to modulate the electronic structures of Si hybrids remains vastly elusive. This study uncovers a redox-controlled stabilization effect exclusive to silicon electrodes functionalized with monolayers that are derived from perylene bisimide (PBI) nanoaggregates. For this class of n-type hybrid nanomaterials, we highlight that the cathodic potential required to inject negative charge carriers into the conduction band of the PBI monolayer can be reversibly stabilized by more than 375 mV through modulation of the maximum anodic potential (MAP) employed during the anodic cycle (i.e., +0.5 or +1.5 V vs Ag/AgCl). The magnitude of this redox-controlled stabilization effect is shown to be dictated by the structure−function relationships of the PBI nanoaggregates exploited to construct the monolayers on Si electrodes. Using a set of control experiments, we demonstrate that such a redox-controlled stabilization effect is not observed for monolayers derived from molecularly dissolved PBI precursors and for Si electrode precursors that feature a low density of anchoring groups. Supported by density functional theory calculations that highlight a significant structural reorganization of a model, partially p-doped PBI nanoaggregates, the data presented herein indicate that a MAP of +1.5 V versus Ag/AgCl is accompanied by a structural reorganization of the monolayers built exclusively from PBI π-aggregates. We propose that conformational perturbations engendered at a high anodic potential (+1.5 V) lead to the emergence of electronic states that further facilitate electron injections. The results uncovered herein establish a proof of principle that transferring the structure−function relationships of π-aggregates on inorganic electrodes delivers a powerful method to construct nanoscale semiconducting interfaces whose conduction band energies are redox-controlled in a reversible manner. This effect may establish the foundation for a new class of memory effect as the anodic potentials (write) dictate the current density at a given cathodic potential (read).

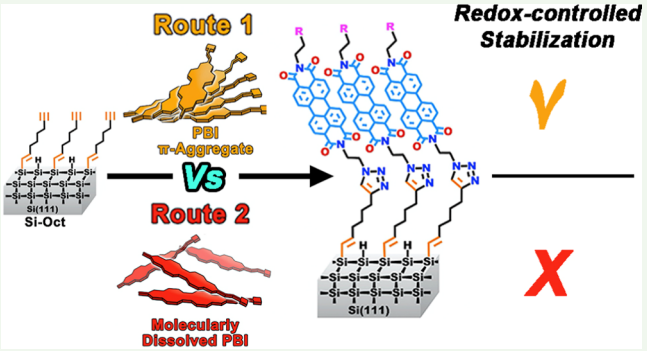

KEYWORDS: *silicon electrode, perylene bisimide, semiconducting monolayers, supramolecular chemistry, surface functionalization*

INTRODUCTION

The tunable optical and electronic properties of organic nanomaterials make them ideal candidates to construct integrated systems pivotal for the interrogation of light−matter interactions, charge-transfer reactions, and charge- and spin-transport processes.[1−10] The performance of these devices is predominantly governed by the inherent nature of the hybrid nanoscale interfaces formed between organic semiconducting domains and inorganic electrodes.[11−16] Consequently, the last few decades have witnessed the emergence of "bottom-up" approaches that capitalize on the functionalization of (semi)-conducting electrode surfaces with redox-active units.[17−19] Although redox-responsive hybrid nanointerfaces constructed in this manner have primarily served as platforms to probe interfacial electron-transfer processes, they have also been exploited to construct molecular electronic junctions, micro-electronic devices, electron-spin filters, and electrochemical biosensors.[15,20−25]

The covalent grafting of redox-active building blocks on hydrogen-terminated monocrystalline silicon (Si−H) electrode surfaces enables the engineering of electroactive nanostructures at the Si/organic interfaces that are structurally well-defined and robust.[17−19] Pioneering studies have unequivocally divulged that the electrochemical properties of hybrid Si/

Received: June 5, 2021
Accepted: July 28, 2021
Published: August 23, 2021

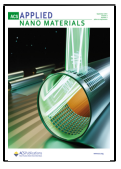

https://doi.org/10.1021/acsanm.1c01473
ACS Appl. Nano Mater. 2021, 4, 8813–8822

organic interfaces are dictated by the electronic structure and the surface density of the redox-active chromophores comprising the monolayers.[19,26−28] Furthermore, synthetic design principles and covalent grafting approaches are leveraged to deliver functional electronic platforms at nanoscale dimension with tunable semiconducting properties.[29−36] For example, seminal studies by Fabre and Hapiot et al. have revealed that in an extremely packed monolayer of ferrocene-derived redox units grafted on Si surfaces (with surface coverage as high as 3.5×10^{-10} mol cm^{-2}), neighboring ferrocene units are involved in significant electronic interactions as validated from scanning electrochemical microscopy analysis.[37] The origin of such high surface density is attributed to the influence of both surface confinement effects as well as the presence of structurally robust Si−C bonds at the interfaces. While hybrid Si−organic interfaces that feature monolayers of organic electron donor modules (p-type) have been extensively investigated, the functionalization of Si surfaces with electron acceptor units (n-type) is restricted to only a handful of studies.[35,36] However, the molecular engineering of n-type interfaces is needed to construct hybrid materials relevant to solar fuel production and organic electronics such as molecular p−n junctions and circuit elements.[38−43]

The assembly properties of nanoaggregates based on perylene bisimide (PBI) cores have been a subject of comprehensive investigation during the last few decades.[44−46] In addition, the low-lying first reduction potentials of PBI units combined with strong absorptivity in the visible part of the spectral window have been leveraged to engineer solvated nanoscale objects and solid-state nanomaterials with which to probe light−matter interaction processes and interrogate charge-transport properties in hierarchical soft matters.[44,46,47] Noncovalent interactions between PBI chromophores in solution enable the formation of superstructures equipped with (opto)electronic properties that are highly sensitive to the conformation of the building blocks.[46,48−53] Seminal studies have unambiguously demonstrated that Ångstrom-level displacements between neighboring PBI units engender severe perturbation of the coulombic and charge-transfer coupling resulting in profound modification of the photophysical and potentiometric properties of PBI superstructures.[54−56] Surprisingly, the extent to which the structure−function properties of PBI nanoaggregates can be derived to tune the semiconducting properties of hybrid Si nanointerfaces remains unexplored. We posit that functionalized silicon surfaces that feature a high surface density of anchoring groups can be leveraged to confine solvated PBI π-aggregates at the organic/inorganic interfaces and deliver a new class of n-type nanomaterials equipped with neoteric electronic functionality.

In the present contribution, we demonstrate that the covalent functionalization of conducting Si electrodes with the neutral **PBI-C_2Am-C_2Az** and cationic **PBI-C_2Am$^+$-C_2Az** PBI units shown in Scheme 1 delivers novel hybrid Si nanointerfaces (**PBI-Sis**) whose conduction band energies can be redox-controlled. Specifically, we show that the potentials required to inject electrons (cathodic potentials) into the conduction band of monolayers derived from PBI π-aggregates are synergistically related to the maximum anodic potential (MAP) used during the oxidation cycle. For a PBI monolayer constructed using **PBI-C_2Am-C_2Az** π-aggregates, while a MAP of +0.5 V initiates a first reduction potential at −0.450 V versus Ag/AgCl, increasing the MAP to +1.5 V facilitates electron injection by more than 375 mV when sweeping back toward the cathodic potentials. Notably, this process is replicated with fidelity by alternating between the two MAPs, that is, +0.5 and +1.5 V, respectively. Furthermore, this redox-controlled stabilization is not observed for nanointerfaces built from molecularly dissolved PBI precursors and Si electrode precursors that feature a low density of anchoring groups. Supported by density functional theory (DFT) calculations that highlight a significant structural reorganization of a model, partially p-doped PBI nanoaggregate, the data presented herein suggest that a MAP of +1.5 V is accompanied with a structural reorganization of the monolayers built exclusively from solvated PBI π-aggregates. We propose that conformational perturbations engendered at a high anodic potential (+1.5 V) lead to the emergence of electronic states that further facilitates electron injections into the conduction band of the monolayers.

Scheme 1. Synthetic Routes to Access PBI-Functionalized Hybrid Si(111) Nanointerfaces (PBI-Sis) via the Azide−Alkyne "Click" Reaction of an Alkyne-Terminated Si Interface (Si-Oct) with PBI-Derived Neutral (PBI-C_2Am-C_2Az) and Cationic (PBI-C_2Am$^+$-C_2Az) Molecular Modules[a]

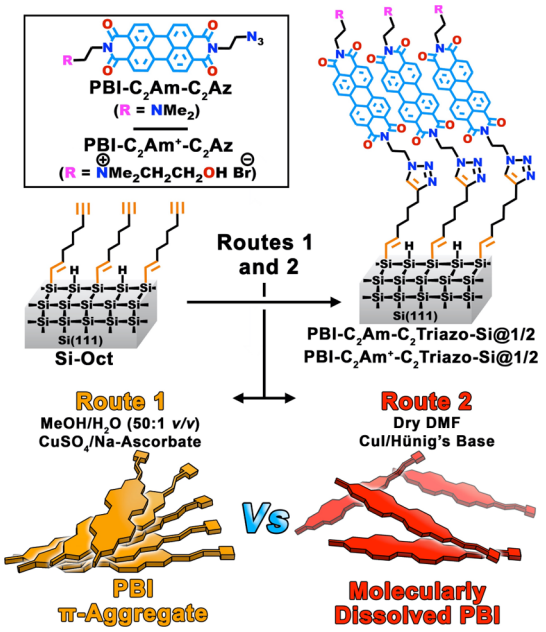

[a]The routes **1** and **2** provide a synthetic handle to modulate the aggregation state of the PBI building blocks during the formation of the monolayers on **Si-Oct**.

RESULTS AND DISCUSSION

The two asymmetric building blocks **PBI-C_2Am-C_2Az** and **PBI-C_2Am$^+$-C_2Az** shown in Scheme 1 have been engineered to tune the amphiphilic character of the PBI units and engender π-conjugated nanoscale objects that exhibit strong and weak excitonic coupling, respectively. These PBI building blocks were accessed via a multistep synthetic pathway that involves sequential base-catalyzed ring-opening and acid-catalyzed ring-closure reactions using perylene-3,4,9,10-tetracarboxylic bisanhydride (PBA) as the starting material (refer to Section 2 of the Supporting Information for details). The lack of ammonium functionality on the **PBI-C_2Am-C_2Az** building

https://doi.org/10.1021/acsanm.1c01473
ACS Appl. Nano Mater. 2021, 4, 8813−8822

block decreases its solubility in polar, protic solvents. This structural attribute affords formation of solvated π-aggregates whose structure−function relationships differ from those elucidated for the **PBI-C_2Am$^+$-C_2Az** π-aggregates. Figure 1A,B shows the ground-state electronic absorption spectra

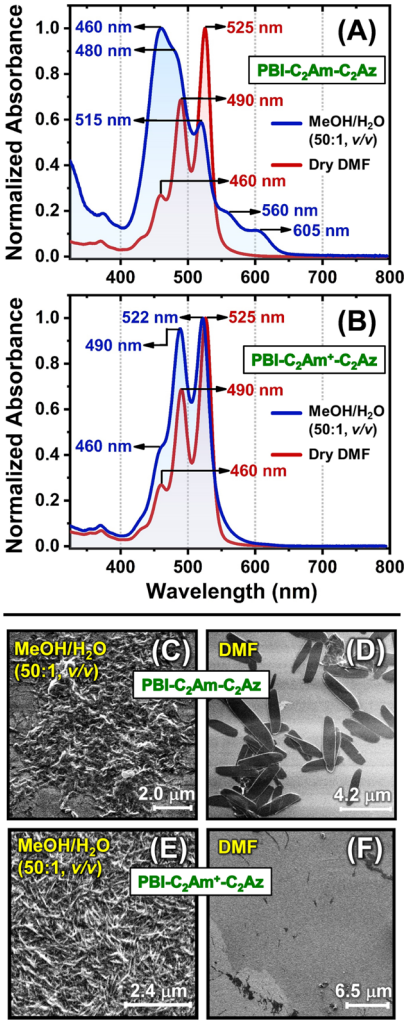

Figure 1. (A,B) Ground-state EAS recorded for the solutions of (A) **PBI-C_2Am-C_2Az** and (B) **PBI-C_2Am$^+$-C_2Az** in MeOH/H_2O (50:1, v/v) and dry DMF. Experimental conditions: [PBI] = 0.7 mM; optical pathlength = 2 mm; temperature = 25 °C. (C−F) Comparative scanning electron microscopy (SEM) images that describe the solid-state morphologies of (C,D) **PBI-C_2Am-C_2Az** and (E,F) **PBI-C_2Am$^+$-C_2Az** recorded for the samples prepared by drop-casting solutions (0.7 mM) of the PBIs in (C,E) MeOH/H_2O (50:1, v/v) and (D,F) dry DMF on untreated Si/SiO_x substrates.

(EAS) recorded in dimethylformamide (DMF) and MeOH/H_2O (50:1 v/v) for the **PBI-C_2Am-C_2Az** and **PBI-C_2Am$^+$-C_2Az** derivatives, respectively. As expected, these two building blocks feature the hallmark of molecularly dissolved species in DMF as confirmed by (1) the well-resolved 0−0, 0−1, and 0−2 vibronic transitions centered at 525, 490, and 460 nm, respectively, that are consistently separated by 169 meV (1360 cm^{-1}; the C=C stretching frequency), and (2) the ratio of intensities of the 0−0 and 0−1 vibronic transitions (1.46) indicates a lack of short- and long-range coupling between PBI units.[51,55,56]

In marked contrast, the spectroscopic signatures recorded for the **PBI-C_2Am-C_2Az** building block in a solution of MeOH/H_2O (50:1, v/v) shown in Figure 1A differ to those evidenced for the DMF solution. Notably, two bathochromically shifted shoulder bands are observed at 605 and 560 nm in addition to the higher energy bands at 515, 480, and 460 nm that are attributed to the 0−0, 0−1, and 0−2 transitions of π-aggregates. While the high-energy bands diagnose the formation of H-like aggregates, the low-energy shoulders may also signal the coexistence of J-like aggregates, although at a smaller concentration.[55,56] It is noteworthy that in the case of the solution of **PBI-C_2Am$^+$-C_2Az** in MeOH/H_2O (50:1, v/v), the EAS shown in Figure 1B (blue trace) reveal virtually identical peak positions of the 0−0 (522 nm), 0−1 (490 nm), and 0−2 (460 nm) vibronic transitions as compared to those characterizing the molecularly dissolved PBI units in the DMF solvent (Figure 1B, red trace). However, the ratio of intensities of the 0−0 and 0−1 vibronic transitions in the MeOH/H_2O mixture appears to be closer to one (1.04). Therefore, it is reasonable to anticipate that the **PBI-C_2Am$^+$-C_2Az** chromophores, in the MeOH/H_2O binary solvent mixture, exist in the form of solubilized, partially aggregated species.

To further highlight how the side-chain functionalities flanked on the two PBI molecular structures impact non-covalent interactions between the π-conjugated cores, the solid-state morphologies of drop-cast **PBI-C_2Am-C_2Az** and **PBI-C_2Am$^+$-C_2Az** solutions were recorded using SEM (cf. Section 5 in the Supporting Information for details). As highlighted in Figure 1C,E, the **PBI-C_2Am-C_2Az** and **PBI-C_2Am$^+$-C_2Az** building blocks share similar solid-state morphologies when deposited from a MeOH/H_2O (50:1, v/v) parent solution. Both enable the formation of fiber-like materials spanning the nano-to-microscale dimension. While the spectroscopic features evidenced by **PBI-C_2Am-C_2Az** and **PBI-C_2Am$^+$-C_2Az** building blocks at a concentration of 0.7 mM in MeOH/H_2O (50:1, v/v) solution signal the formation of electronically disparate nanoaggregate species, the fact that they engender virtually identical hierarchical nano-to-microscale superstructures may stem from a concentration effect during the drop-casting process. In sharp contrast, the SEM images of the sample drop-cast from a solution of **PBI-C_2Am-C_2Az** in DMF (Figures 1D and S8 and S9) reveal the presence of isolated and well-defined 2D microstructures whose lengths and heights vary within the range of 4−5 μm and 40−50 nm, respectively. Furthermore, the sample drop-cast from the solution of **PBI-C_2Am$^+$-C_2Az** in DMF lacks the ability to organize into structures with hierarchical features in the solid state as evidenced by the SEM images shown in Figures 1F and S11. A similar observation has been made for analogous, cationic PBI derivatives.[48,49,51]

Interrogating the potentiometric properties of the **PBI-C_2Am-C_2Az** units as molecularly dissolved species in DMF and as solvated π-aggregates in MeOH/H_2O (50:1, v/v) reveals striking electronic structure disparities. Please note that all potentials are reported against Ag/AgCl. While the cyclic voltammograms (CVs) recorded for the **PBI-C_2Am-C_2Az** units in the DMF solvent (Figures 2B and S12B) evidence reversible electrochemical signals assigned to the first and second reduction of the redox-active PBI cores,[57,58] the CVs of the solvated π-aggregates shown in Figures 2A and S12A highlight nonreversible redox processes as indicated by a large peak-to-peak separation ($\Delta E^{(p)}$ > 390 mV) between the cathodic ($E^{(p1)}$) and anodic peak potentials ($E^{(p2)}$). This

https://doi.org/10.1021/acsanm.1c01473
ACS Appl. Nano Mater. 2021, 4, 8813−8822

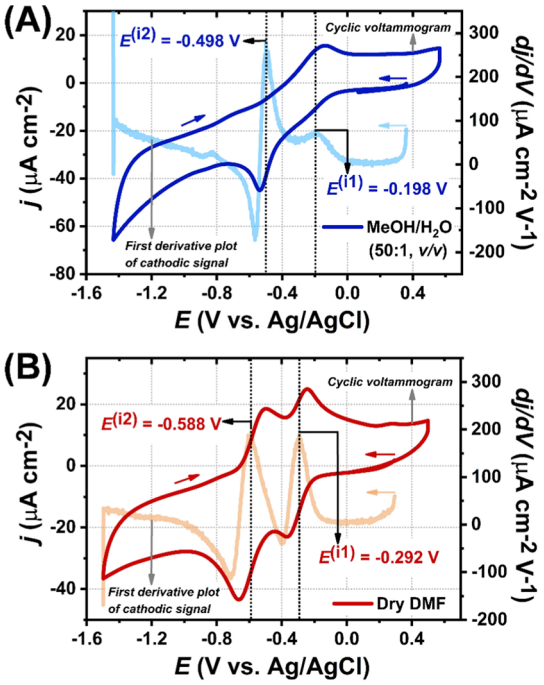

Figure 2. CVs (scan rate = 0.05 V s^{-1}) recorded for the solutions (concentration = 0.7 mM) of **PBI-C_2Am-C_2Az** in (A) MeOH/H_2O (50:1, v/v) and (B) dry DMF using *n*-Bu_4NPF_6 (0.7 mM) as the supporting electrolyte. Note the inflection potentials of reduction as determined from the first derivative plots of the cathodic signals. Experimental conditions employed glassy carbon as the working electrode (electro-active surface area = 0.071 cm^2), Ag/AgCl (3 M NaCl) as the reference electrode, and Pt as the counter electrode under an Ar gas atmosphere at 25 °C.

observation originates from slow electron rate processes and structural reorganization of the solvated nanoaggregates upon reduction and back-oxidation, similar to recently reported findings in other systems.[36,59,60] To gain more insights into the potentiometric properties of the **PBI-C_2Am-C_2Az** π-aggregates, the first cathodic inflection potential ($E^{(i1)}$) was evaluated by plotting the first derivative of the CV when sweeping toward the cathodic side.[61] This approach established by Vullev and co-workers allows for the estimation of the half-wave potential ($E^{(1/2)}$) for electrochemical systems that deviate from reversibility. As chronicled in Figures 2A and S12A, the **PBI-C_2Am-C_2Az** π-aggregates are characterized by a first reduction potential ($E^{(i1)}$ = −0.198 V) that is stabilized by more than 90 mV as compared to that recorded for the molecularly dissolved **PBI-C_2Am-C_2Az** units ($E^{(i1)}$ = −0.292 V). A second reduction potential $E^{(i2)}$ centered at −0.498 V is recorded for the π-aggregates (Figure 2A) and suggests the formation of heavily n-doped species.[62]

The CVs recorded for the **PBI-C_2Am$^+$-C_2Az** π-aggregates and the molecularly dissolved analogues are shown in Figure S13. While the electrochemical signals recorded for the **PBI-C_2Am$^+$-C_2Az** π-aggregates formed in MeOH/H_2O (50:1, v/v) share some resemblance to those elucidated for the **PBI-C_2Am-C_2Az** π-aggregates, the former evidences the first reduction potential ($E^{(i1)}$ = −0.270 V) destabilized by more than 70 mV with respect to that recorded for the latter ($E^{(i1)}$ = −0.198 V). The apparent stabilization of the first reduction potential unraveled for the **PBI-C_2Am-C_2Az** π-aggregates suggests that the interchromophore interaction varies, to some extent, with respect to the interactions which characterize the **PBI-C_2Am$^+$-C_2Az** π-aggregates. This conclusion corroborates the observation made from the electronic spectral properties of the nanoaggregates where a higher degree of electronic coupling has been highlighted in the **PBI-C_2Am-C_2Az** assemblies.

By exploiting route 1 in Scheme 1, functionalization of the **Si-Oct** interface precursor with the **PBI-C_2Am-C_2Az** and **PBI-C_2Am$^+$-C_2Az** π-aggregates delivers the **PBI-C_2Am-C_2Triazo-Si@1** and **PBI-C_2Am$^+$-C_2Triazo-Si@1** semiconducting nanointerfaces, respectively. The Si interfaces constructed from molecularly dissolved PBI units (route 2, Scheme 1), namely, **PBI-C_2Am-C_2Triazo-Si@2** and **PBI-C_2Am$^+$-C_2Triazo-Si@2**, offer control platforms against which to investigate the effect of PBI-aggregated states on the final potentiometric properties of the Si nanohybrids. Please refer to Section 3A in the Supporting Information for synthetic details. To analyze the solid-state morphologies characterizing these four interfaces, tapping mode atomic force microscopy (AFM) was exploited. The corresponding AFM images recorded for the **PBI-C_2Am-C_2Triazo-Si@1** and **PBI-C_2Am$^+$-C_2Triazo-Si@1** nanohybrids are shown in Figures 3A and S16A, respectively, and reveal the

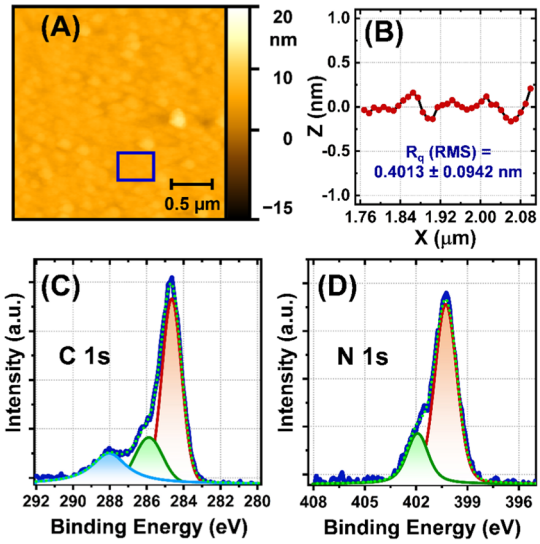

Figure 3. (A) Tapping mode AFM topographic image of the **PBI-C_2Am-C_2Triazo-Si@1** interface. (B) Cross section profile of the area within the inset of the AFM image (blue square) in (A) to calculate the R_q (RMS) roughness of the surface. (C,D) High-resolution XPS spectra (navy blue), deconvoluted spectra (red/green/sky blue), and cumulative/fitted spectra (dotted green) of the **PBI-C_2Am-C_2Triazo-Si@1** interface that represent the C 1s (C) and N 1s (D) areas.

existence of smooth monolayer surfaces. Further quantification of the root-mean square surface roughness parameter, R_q (RMS), further supports this claim as the R_q value is below 0.5 nm. Please refer to Figures 3B and S16. An identical observation is made for the **PBI-C_2Am-C_2Triazo-Si@2** and **PBI-C_2Am$^+$-C_2Triazo-Si@2** nanointerfaces whose AFMs and associated R_q values are shown in Figures S15 and S17, respectively.

To confirm the covalent anchorage of the PBI units on the Si electrode, atomic compositions of the four engineered semiconducting nanointerfaces were interrogated using X-ray photoelectron spectroscopy (XPS). Details are provided in Section 8 of the Supporting Information. The representative high-resolution XPS spectra of the C 1s and N 1s areas for

https://doi.org/10.1021/acsanm.1c01473
ACS Appl. Nano Mater. 2021, 4, 8813−8822

PBI-C_2Am-C_2Triazo-Si@1 are shown in Figure 3C,D, respectively. The emission feature of the C 1s signal is deconvoluted into three Voigt functions with the peaks centered at binding energies of 288.0, 285.9, and 284.6 eV. While the high-energy emission signal at 288.0 eV is the spectroscopic signature of oxygen-bonded carbon (C═O) atoms, the peaks centered at 285.9 and 284.6 eV are diagnostic of nitrogen-bonded carbon (C−N) and carbon-bonded carbon (C−C/C═C) atoms, respectively. Because C 1s signals may present some contamination from external carbon sources, specifically, C−O bonds giving rise to an emission signal centered at 286 eV, the high-resolution N 1s XPS spectrum shown in Figure 3D is a more adequate spectroscopic handle to unambiguously confirm the attachment of the PBI building blocks. This N 1s emission feature shown in Figure 3D is deconvoluted using two Voigt functions centered at 402.1 and 400.1 eV, attesting the existence of chemically disparate nitrogen atoms. The XPS characterization of the **PBI-C_2Am-C_2Triazo-Si@2** and the **PBI-C_2Am$^+$-C_2Triazo-Si@1-2** interfaces is discussed in Section 8 of the Supporting Information, and it confirms the attachment of the PBI units on the **Si-Oct** precursor.

The potentiometric properties of the **PBI-Si** hybrid nanointerfaces built from PBI π-aggregates, namely, **PBI-C_2Am-C_2Triazo-Si@1** and **PBI-C_2Am$^+$-C_2Triazo-Si@1** in Scheme 1, differ markedly to those recorded for the Si nanointerfaces constructed from molecularly dissolved PBI units, that is, **PBI-C_2Am-C_2Triazo-Si@2** and **PBI-C_2Am$^+$-C_2Triazo-Si@2**. Please refer to Section 9 of the Supporting Information. Figure 4A,B compares the CVs of **PBI-C_2Am-C_2Triazo-Si@1** recorded as a function of the MAPs applied during the anodic sweeps. Additional CVs with more details are shown in Figures S29 and S30. The CVs shown in Figure 4A (MAP = +0.5 V) exhibit broad, weakly resolved, and ill-defined redox waves recorded during the excursions toward the cathodic and anodic potentials. While the irreversible character of the probed nanointerfaces originates from slow electron-transfer rate constants and structural reorganizations occurring at the monolayer level,[63−68] the CVs are nonetheless reproducible and indicate negligible surface damage under the experimental conditions being employed. It is interesting to note that a modest cathodic shift of the initial first reduction potential ($E^{(i1)}_{Cycle\ 1}$ = −0.390 V) occurs during cycle 2 and 3 ($E^{(i1)}_{Cycle\ 2}$ = −0.450 V, $E^{(i1)}_{Cycle\ 3}$ = −0.450 V). This shift highlights conformational changes of the PBI monolayers taking place during the first cathodic sweep (cycle 1). In marked contrast, Figure 4B shows that excursion to a MAP of +1.5 V has a drastic impact on the cathodic wave whose first reduction potential ($E^{(i1)}_{Cycle\ 2}$ = −0.075 V) is stabilized by more than 375 mV as compared to the reduction potential recorded in cycle 2 when using MAP = +0.5 V ($E^{(i1)}_{Cycle\ 2}$ = −0.450 V). It is interesting to note that when utilizing a MAP of +1.5 V, (1) the $E^{(i1)}_{Cycle\ 1}$ recorded during the first cathodic sweep that starts from a potential of 0.5 V exhibits a similar value to that recorded for a MAP of +0.5 V (Figure 4A), (2) the apparent stabilization of the first reduction potential is selectively controlled by MAP = +1.5 V, and (3) an additional cycle using a MAP of +1.5 V (cycle 3, Figure 4B) enforces identical stabilization of the first reduction potential ($E^{(i1)}_{Cycle\ 3}$ = −0.090 V). As shown in Figure S39, this process is reversible; the $E^{(i1)}$ recorded with the **PBI-C_2Am-C_2Triazo-Si@1** nanointerface can be restored to its original value by setting the MAP to +0.5 from +1.5 V. Because the cathodic potentials required to n-

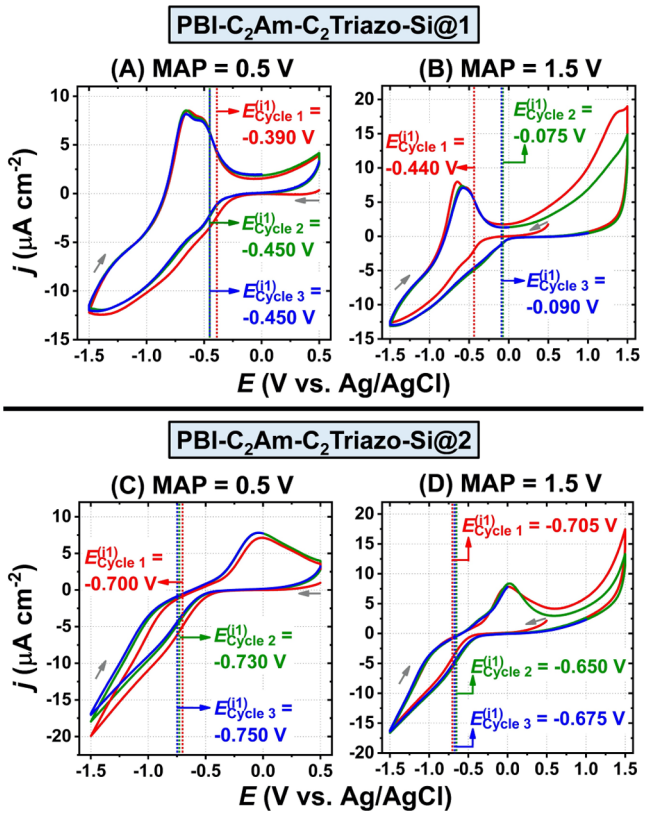

Figure 4. CVs (cycles 1−3; scan rate = 0.05 V s^{-1}) of **PBI-C_2Am-C_2Triazo-Si@1** (A,B) and **PBI-C_2Am-C_2Triazo-Si@2** (C,D) interfaces recorded using a starting potential of +0.5 V in cycle 1 and the MAP limit of +0.5 V (A,C) and +1.5 V (B,D) for cycle 2/3 in dry acetonitrile in the presence of *n*-Bu_4NPF_6 as the supporting electrolyte. Experimental conditions employed the **PBI-Si** surfaces as the working electrodes (electro-active surface area = 0.5026 cm^2), Ag/AgCl (3 M NaCl) as the reference electrode, and Pt as the counter electrode under an Ar gas atmosphere at 25 °C. Please note that (i) the starting potential of cycle 1 in all the cases is +0.5 V; (ii) cycles 1, 2, and 3 are represented in red, green, and blue color, respectively, and (iii) $E^{(i1)}$ potentials are shown for the three consecutive cycles.

dope the PBI monolayers are modulated by the anodic potentials, we interpret this observation as a redox-controlled stabilization effect of the monolayer conduction band. This effect is also observed for the hybrid **PBI-C_2Am$^+$-C_2Triazo-Si@1** nanointerface derived from PBI nanoaggregates, although at a lower magnitude. As shown in Figures S33 and S34, the first reduction potential recorded after excursion to a MAP of +1.5 V ($E^{(i1)}_{Cycle\ 2}$ = −0.220 V) is stabilized by ∼ 240 mV with respect to that observed when a MAP = +0.5 V is exploited ($E^{(i1)}_{Cycle\ 2}$ = −0.460 V). As chronicled in Figure S41, the redox-controlled stabilization effect on the cathodic potentials of **PBI-C_2Am$^+$-C_2Triazo-Si@1** is also found to be reversible upon setting the MAP from +1.5 to +0.5 V.

In contrast, the redox-controlled stabilization effect is absent for hybrid Si nanointerfaces built from molecularly dissolved PBI units. As shown in Figures 4C,D and S35 and 36 that chronicle the CVs recorded for the **PBI-C_2Am-C_2Triazo-Si@2** and **PBI-C_2Am$^+$-C_2Triazo-Si@2** nanohybrids, respectively, the MAP (+0.5 and +1.5 V) has no impact on the first reduction potentials. For instance, during the analysis of **PBI-C_2Am-C_2Triazo-Si@2**, a MAP of +0.5 V is associated with $E^{(i1)}_{Cycle\ 1}$ = −0.700 V and $E^{(i1)}_{Cycle\ 2}$ = −0.730 V (Figure 4C), while

https://doi.org/10.1021/acsanm.1c01473
ACS Appl. Nano Mater. 2021, 4, 8813−8822

similar reduction potentials (±50 mV) are recorded when using a MAP of +1.5 V (Figure 4D). It is interesting to note that the potentials required to inject negative charge carriers into the conduction band of the **PBI-C_2Am-C_2Triazo-Si@2** monolayer ($E^{(i1)}_{Cycle\ 1}$ = −0.700 V) are more negative than those recorded for the **PBI-C_2Am$^+$-C_2Triazo-Si@2** ($E^{(i1)}_{Cycle\ 1}$ = −0.405 V). This observation diagnoses a nanointerface conformation that differs to that characterizing the **PBI-C_2Am$^+$-C_2Triazo-Si@2** analogue. This assumption is supported by the solid-state morphologies evidenced by the **PBI-C_2Am-C_2Az** and **PBI-C_2Am$^+$-C_2Az** units drop-cast from DMF solutions. As shown in Figure 1D, the neutral PBI units enable the formation of 2D nanosheets, whereas the charged species lacks the ability to evolve into higher ordered nanostructures in the solid state (Figure 1F).

Because the redox-controlled stabilization effect is exclusive to interfaces constructed from PBI nanoaggregates, we hypothesized that the aggregation state of the initial PBI units, in solution, dictates the structure−function relationships of the monolayers covalently anchored on Si electrodes. To further support this hypothesis, the **PBI-C_2Am-C_2Az** π-aggregates were anchored on the Si surface **Si-Oct(1:50)**, a surface which is characterized by a low density of reactive alkyne groups, 8.4 × 10^{-12} mol cm^{-2}. Refer to Section 3B in the Supporting Information for more details on the synthesis of the **PBI-C_2Am-C_2Triazo-Si(1:50)@1** nanointerface. In addition, tapping mode AFM images and high-resolution XPS spectra are shown in Figures S18 and S23, respectively. Since this surface density corresponds to a coverage of one alkyne per 20 nm^2,[36] it is fair to assume that lateral interaction between PBI units is suppressed in the hybrid **PBI-C_2Am-C_2Triazo-Si(1:50)@1** nanointerface. Congruent with this expectation, the corresponding CVs shown in Figures S37 and S38 reveal dramatically disparate potentiometric properties as compared to those highlighted previously for the **PBI-C_2Am-C_2Triazo-Si@1** nanohybrid. Starting at +0.5 V, the cycle toward a final cathodic potential of −1.5 V (cycle 1) unravels an irreversible electrochemical signal characterized by an $E^{(i1)}_{Cycle\ 1}$ of −0.800 V (Figure S37). No distinguishable redox waves are discerned when sweeping back to a MAP of +0.5 V. Surprisingly, an apparent cathodic shift of the first reduction potential is observed during cycle 2 ($E^{(i1)}_{Cycle\ 2}$ = −1.02 V) which is reproduced during cycle 3. As shown in Figure S38, switching the MAP to +1.5 V engenders cathodic electrochemical signals that share some similarities ($E^{(i1)}_{Cycle\ 2}$ = −1.04 V) to those recorded during the second cycle using MAP = +0.5 V. This data indicates that the **PBI-C_2Am-C_2Triazo-Si(1:50)@1** nanohybrids, characterized with a low density of PBI units, do not evidence the redox-controlled stabilization effect observed for the **PBI-C_2Am-C_2Triazo-Si@1** and **PBI-C_2Am$^+$-C_2Triazo-Si@1** semiconducting nanointerfaces.

The redox-controlled stabilization effect recorded for the **PBI-C_2Am-C_2Triazo-Si@1** and **PBI-C_2Am$^+$-C_2Triazo-Si@1** nanointerfaces is postulated to originate from the formation of electronic states engendered at MAP = +1.5 V, in monolayers exclusively derived from PBI nanoaggregates. The origin of these nascent trap states can be rationalized by structural deformations of the PBI monolayer enforced at a high anodic potential. While the oxidation of molecularly dissolved PBI units has been reported at a potential of +1.60 V versus SCE,[69,70] the oxidation potential of the confined PBI units on the silicon electrode in the **PBI-C_2Am-C_2Triazo-Si@1** nanohybrid may differ, to some extent, to that evidenced in a solvated environment. In this regard, a MAP of +1.5 V can enable the injection of positive charge carriers (holes) into the valence bands of the PBI nanoaggregates anchored on the silicon surface. As shown in Figure 4B, an anodic peak centered at +1.35 V is discerned during the sweep to +1.5 V in cycle 1. This signal may correspond to the injection of the positive charge carriers in the monolayer derived from **PBI-C_2Am-C_2Az** nanoaggregates. In contrast, this anodic peak is absent when probing monolayers derived from molecularly dissolved PBI as seen in the CVS in Figure 4D.

Energy-minimized structures of a model nanoaggregate, a trimer π-stack, as a function of p-doping levels have been computed at the DFT level of theory and are shown in Figure 5. Please refer to Section 10 of the Supporting Information for

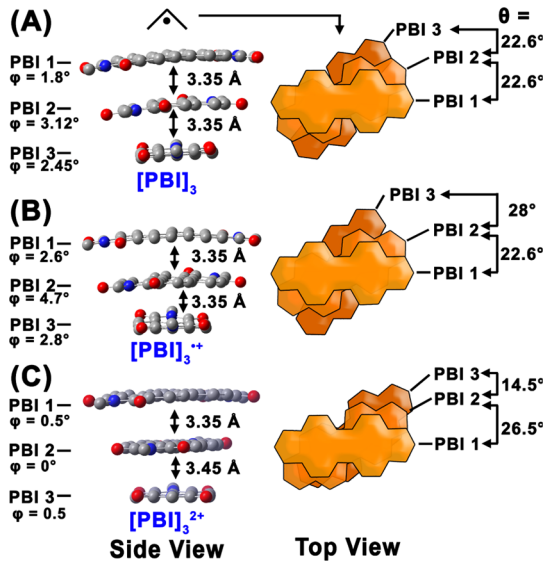

Figure 5. Energy-minimized structures computed at the DFT level of theory (ωB97X-D) for the model PBI trimer stacks as a function of hole concentration. (A) Neutral PBI stack $[PBI]_3$, (B) one hole per PBI stacks $[PBI]_3^{\bullet+}$, (C) two holes per PBI stacks $[PBI]_3^{2+}$. For each trimer, the dihedral angle (θ) defines the offset between two PBI monomers, while the dihedral angle (φ) defines the twist of the bay region and is measured using positions 6, 6A, 7, and 7 A of the PBI core. Details are given in the Section 10 of the Supporting Information.

details. Non-negligible structural modifications accompany the formation of the p-doped species $[PBI]_3^{\bullet+}$ and $[PBI]_3^{2+}$ as compared to the neutral precursor $[PBI]_3$. Specifically, the dihedral angle (θ) between PBI 3 and PBI 2 in the monocationic $[PBI]_3^{\bullet+}$ trimer increases ($\Delta\theta \sim 5°$) as a result of perturbation of the dispersion interactions associated with the oxidation of one PBI unit. Please refer to Figure S48 in the Supporting Information for the detailed electrostatic potential maps. Furthermore, it is interesting to note a non-negligible twist of dihedral angle characterizing the bay region (φ) of the PBI units in the monocation $[PBI]_3^{\bullet+}$ trimer in addition to the bending of the PBI cores along their long molecular axis (Figure S47). Further p-doping of $[PBI]_3^{\bullet+}$ to $[PBI]_3^{2+}$ is accompanied by (1) a decrease of the dihedral angle between PBI 2 and PBI 3 ($\Delta\theta \sim 13.5°$), while an increase in dihedral angle between PBI 1 and PBI 2 is witnessed ($\Delta\theta \sim 4°$), (2) an increase in the interchromophoric distance between PBI 2 and PBI 3, and (3) a concurrent planarization of the PBI cores, as summarized in Figure S48. Analysis of these energy-minimized

https://doi.org/10.1021/acsanm.1c01473
ACS Appl. Nano Mater. 2021, 4, 8813−8822

stack models confirms that non-negligible structural perturbation accompanies the p-doping of the nanoaggregates.

We propose that the structural perturbation enforced during the partial p-doping of the PBI monolayers in **PBI-C_2Am-C_2Triazo-Si@1** and **PBI-C_2Am^+-C_2Triazo-Si@1** nanohybrids at MAP = +1.5 V may be preserved, to some degree, when sweeping back toward the cathodic potentials. We postulate that this structural reconfiguration is associated with the formation of electronic trap states that assist electron injection into the PBI monolayers at lower cathodic potentials. The fact that the **PBI-C_2Am^+-C_2Triazo-Si@1** nanointerface demonstrates a redox-controlled stabilization effect of the conduction band energy less pronounced than that observed for the **PBI-C_2Am-C_2Triazo-Si@1** analogue further underscores the noninnocent role played by the PBI π-aggregate precursors in dictating the semiconducting properties of functionalized Si electrodes. As shown by ground-state electronic absorption spectroscopy (Figure 1B), **PBI-C_2Am^+-C_2Az** building blocks evidence the hallmark of weakly coupled H-like aggregates in MeOH/H_2O (50:1, v/v). In contrast, the spectroscopic signatures of the **PBI-C_2Am-C_2Az** π-aggregates in an identical solvent system indicate strong excitonic coupling between the repeating units. Congruent with this observation, it is fair to assume that the PBI monolayers derived from the **PBI-C_2Am-C_2Az** π-aggregates capture some of the structure−function relationships of the nanoaggregate precursors. Consequently, noncovalent interactions between PBI repeating units in the **PBI-C_2Am-C_2Triazo-Si@1** nanointerface differ to those in **PBI-C_2Am^+-C_2Triazo-Si@1** and assist a more pronounced structural perturbation at MAP = +1.5 V. Taken together, these results unravel that the magnitude of the conduction band stabilization controlled by the anodic potentials is intimately related to the interaction of PBI units in the monolayers. To the best of our knowledge, the results uncovered herein establish the first proof of principle that transferring the structure−function relationships of solvated nanoaggregates on inorganic electrodes delivers a powerful method to construct electroactive monolayers whose conduction band energies are redox-controlled in a reversible manner.

CONCLUSIONS

In conclusion, we report the first functionalization of Si electrodes with π-conjugated PBI units that demonstrate various degrees of aggregation. The chemical compositions and structural analyses performed on these semiconducting hybrid nanointerfaces confirm the successful attachment of PBI units and the formation of homogeneous monolayers. Using cyclic voltammetry experiments, the existence of a redox-controlled stabilization effect on the conduction band energies exclusive to Si surfaces functionalized with PBI nanoaggregates is unraveled. For these hybrid materials, the cathodic potential required to n-dope the PBI monolayers can be modulated by tuning the MAPs. Although excursion to a MAP of +0.5 V for the **PBI-C_2Am-C_2Triazo-Si@1** nanointerface derived from neutral PBI nanoaggregates induces a reduction wave at −0.450 V, an anodic potential of +1.5 V enforces a stabilization of more than 375 mV of the first reduction potential ($E^{(i1)}_{Cycle\ 2}$ = −0.075 V) when sweeping back to the cathodic potentials. This process is reversible and can be switched back and forth by regulating the MAP exploited during the anodic sweeps, that is, +0.5 and +1.5 V.

For semiconducting nanointerfaces built from molecularly dissolved PBI precursors, the cathodic potentials necessary to inject negative charge carriers remain invariant regardless of the MAP employed. To unambiguously confirm that the redox-controlled stabilization effect observed at the **PBI-C_2Am-C_2Triazo-Si@1** surface is a result of PBI nanoaggregates, the functionalization of Si surface precursors presenting a low density of anchoring functional groups with PBI nanoaggregates was engineered. Congruent with our hypothesis, this hybrid interface lacks this redox-controlled stabilization effect. Taken together, these control experiments underscore the cardinal role played by the PBI nanoaggregate precursors in modulating novel semiconducting properties to Si hybrid nanomaterials. Furthermore, because the **PBI-C_2Am^+-C_2Az** building blocks demonstrate a lower degree of aggregation than that evidenced by the neutral **PBI-C_2Am-C_2Az** analogue, we posit that the magnitude of the redox-controlled stabilization effect observed in the **PBI-C_2Am-C_2Triazo-Si@1** and **PBI-C_2Am^+-C_2Triazo-Si@1** interfaces correlates with the aggregation state of the PBI precursors. To rationalize the role played by the MAP, DFT calculation performed on a partially p-doped PBI trimer π-stack unravels non-negligible structural deformation that may assist the formation of electronic trap states. These newly formed states facilitate negative charge carrier injections. By uncovering that the structure−function relationships of π-aggregates can be leveraged to regulate the electronic properties of semiconducting interfaces, this study delivers new rules and principles to engineer nanomaterials relevant to energy transduction and information storage. In this regard, the reported redox-controlled stabilization effect may establish the foundation for a new class of memory effect as the anodic potential (write) dictates the current density at a given cathodic potential (read).

ASSOCIATED CONTENT

Supporting Information

The Supporting Information is available free of charge at https://pubs.acs.org/doi/10.1021/acsanm.1c01473.

Synthesis, sample preparation, ground-state EAS, SEM and AFM images, cyclic voltammograms, XPS spectra, NMR spectra, IR spectra, and MS spectra (PDF)

AUTHOR INFORMATION

Corresponding Author

Jean-Hubert Olivier − *Department of Chemistry, University of Miami, Coral Gables, Florida 33146, United States;* orcid.org/0000-0003-0978-4107; Phone: +1 305 284 3279; Email: jh.olivier@miami.edu

Authors

Arindam Mukhopadhyay − *Department of Chemistry, University of Miami, Coral Gables, Florida 33146, United States;* orcid.org/0000-0002-0620-4157

Kaixuan Liu − *Department of Chemistry, University of Miami, Coral Gables, Florida 33146, United States*

Victor Paulino − *Department of Chemistry, University of Miami, Coral Gables, Florida 33146, United States;* orcid.org/0000-0001-8916-3604

Carrie L. Donley − *Chapel Hill Analytical and Nanofabrication Laboratory, Department of Applied Physical Sciences, University of North Carolina, Chapel Hill, North*

https://doi.org/10.1021/acsanm.1c01473
ACS Appl. Nano Mater. 2021, 4, 8813−8822

Carolina 27599, United States; orcid.org/0000-0003-0906-306X

Complete contact information is available at: https://pubs.acs.org/10.1021/acsanm.1c01473

Author Contributions

The manuscript was written through contributions of all authors. All authors have given approval to the final version of the manuscript.

Notes

The authors declare no competing financial interest.

■ ACKNOWLEDGMENTS

The paper is dedicated to Prof. Michael Therien on the occasion of his 60th Birthday. Our Si surface functionalization work is supported by the Arnold and Mabel Beckman Foundation under award BYI 2018, and our work on redox-assisted assembly of π-conjugated chromophore is supported by the National Science Foundation under the CAREER award CHE-1941410. XPS analysis was performed at the Chapel Hill Analytical and Nanofabrication Laboratory, CHANL, a member of the North Carolina Research Triangle Nanotechnology Network, RTNN, which is supported by the National Science Foundation, Grant CCS-1542015, as part of the National Nanotechnology Coordinated Infrastructure, NNCI.

■ REFERENCES

(1) Wasielewski, M. R. Self-assembly strategies for integrating light harvesting and charge separation in artificial photosynthetic systems. *Acc. Chem. Res.* **2009**, *42*, 1910−1921.
(2) Facchetti, A. π-Conjugated polymers for organic electronics and photovoltaic cell applications. *Chem. Mater.* **2011**, *23*, 733−758.
(3) Göhler, B.; Hamelbeck, V.; Markus, T. Z.; Kettner, M.; Hanne, G. F.; Vager, Z.; Naaman, R.; Zacharias, H. Spin selectivity in electron transmission through self-assembled monolayers of double-stranded DNA. *Science* **2011**, *331*, 894−897.
(4) Faramarzi, V.; Niess, F.; Moulin, E.; Maaloum, M.; Dayen, J.-F.; Beaufrand, J.-B.; Zanettini, S.; Doudin, B.; Giuseppone, N. Light-triggered self-construction of supramolecular organic nanowires as metallic interconnects. *Nat. Chem.* **2012**, *4*, 485−490.
(5) Bloom, B. P.; Liu, R.; Zhang, P.; Ghosh, S.; Naaman, R.; Beratan, D. N.; Waldeck, D. H. Directing charge transfer in quantum dot assemblies. *Acc. Chem. Res.* **2018**, *51*, 2565−2573.
(6) Bullard, G.; Tassinari, F.; Ko, C.-H.; Mondal, A. K.; Wang, R.; Mishra, S.; Naaman, R.; Therien, M. J. Low-resistance molecular wires propagate spin-polarized currents. *J. Am. Chem. Soc.* **2019**, *141*, 14707−14711.
(7) Kulkarni, C.; Mondal, A. K.; Das, T. K.; Grinbom, G.; Tassinari, F.; Mabesoone, M. F. J.; Meijer, E. W.; Naaman, R. Highly Efficient and Tunable Filtering of Electrons' Spin by Supramolecular Chirality of Nanofiber-Based Materials. *Adv. Mater.* **2020**, *32*, 1904965.
(8) Carroli, M.; Dixon, A. G.; Herder, M.; Pavlica, E.; Hecht, S.; Bratina, G.; Orgiu, E.; Samorì, P. Multiresponsive Nonvolatile Memories Based on Optically Switchable Ferroelectric Organic Field-Effect Transistors. *Adv. Mater.* **2021**, *33*, 2007965.
(9) Bai, Y.; Olivier, J.-H.; Yoo, H.; Polizzi, N. F.; Park, J.; Rawson, J.; Therien, M. J. Molecular Road Map to Tuning Ground State Absorption and Excited State Dynamics of Long-Wavelength Absorbers. *J. Am. Chem. Soc.* **2017**, *139*, 16946−16958.
(10) He, X.; Velizhanin, K. A.; Bullard, G.; Bai, Y.; Olivier, J.-H.; Hartmann, N. F.; Gifford, B. J.; Kilina, S.; Tretiak, S.; Htoon, H.; Therien, M. J.; Doorn, S. K. Solvent- and Wavelength-Dependent Photoluminescence Relaxation Dynamics of Carbon Nanotube sp3 Defect States. *ACS Nano* **2018**, *12*, 8060−8070.
(11) Buriak, J. M. Organometallic chemistry on silicon and germanium surfaces. *Chem. Rev.* **2002**, *102*, 1271−1308.
(12) McCreery, R. L. Molecular electronic junctions. *Chem. Mater.* **2004**, *16*, 4477−4496.
(13) Onclin, S.; Ravoo, B. J.; Reinhoudt, D. N. Engineering silicon oxide surfaces using Self-Assembled monolayers. *Angew. Chem., Int. Ed.* **2005**, *44*, 6282−6304.
(14) Love, J. C.; Estroff, L. A.; Kriebel, J. K.; Nuzzo, R. G.; Whitesides, G. M. Self-assembled monolayers of thiolates on metals as a form of nanotechnology. *Chem. Rev.* **2005**, *105*, 1103−1170.
(15) Liu, F.; Luber, E. J.; Huck, L. A.; Olsen, B. C.; Buriak, J. M. Nanoscale plasmonic stamp lithography on silicon. *ACS Nano* **2015**, *9*, 2184−2193.
(16) Belding, L.; Root, S. E.; Li, Y.; Park, J.; Baghbanzadeh, M.; Rojas, E.; Pieters, P. F.; Yoon, H. J.; Whitesides, G. M. Conformation, and Charge Tunneling through Molecules in SAMs. *J. Am. Chem. Soc.* **2021**, *143*, 3481−3493.
(17) Ciampi, S.; Harper, J. B.; Gooding, J. J. Wet chemical routes to the assembly of organic monolayers on silicon surfaces via the formation of Si−C bonds: Surface preparation, passivation and functionalization. *Chem. Soc. Rev.* **2010**, *39*, 2158−2183.
(18) Gooding, J. J.; Ciampi, S. The molecular level modification of surfaces: from self-assembled monolayers to complex molecular assemblies. *Chem. Soc. Rev.* **2011**, *40*, 2704−2718.
(19) Fabre, B. Functionalization of oxide-free silicon surfaces with redox-active assemblies. *Chem. Rev.* **2016**, *116*, 4808−4849.
(20) Dionne, E. R.; Toader, V.; Badia, A. Microcantilevers bend to the pressure of clustered redox centers. *Langmuir* **2014**, *30*, 742−752.
(21) Beiler, A. M.; Khusnutdinova, D.; Wadsworth, B. L.; Moore, G. F. Cobalt porphyrin−polypyridyl surface coatings for photoelectrosynthetic hydrogen production. *Inorg. Chem.* **2017**, *56*, 12178−12185.
(22) Dionne, E. R.; Dip, C.; Toader, V.; Badia, A. Micromechanical Redox Actuation by Self-Assembled Monolayers of Ferrocenylalkanethiolates: Evens Push More Than Odds. *J. Am. Chem. Soc.* **2018**, *140*, 10063−10066.
(23) Wong, R. A.; Yokota, Y.; Wakisaka, M.; Inukai, J.; Kim, Y. Discerning the Redox-Dependent Electronic and Interfacial Structures in Electroactive Self-Assembled Monolayers. *J. Am. Chem. Soc.* **2018**, *140*, 13672−13679.
(24) Wadsworth, B. L.; Khusnutdinova, D.; Urbine, J. M.; Reyes, A. S.; Moore, G. F. Expanding the Redox Range of Surface-Immobilized Metallocomplexes Using Molecular Interfaces. *ACS Appl. Mater. Interfaces* **2019**, *12*, 3903−3911.
(25) Park, J.; Belding, L.; Yuan, L.; Mousavi, M. P. S.; Root, S. E.; Yoon, H. J.; Whitesides, G. M. Rectification in Molecular Tunneling Junctions Based on Alkanethiolates with Bipyridine−Metal Complexes. *J. Am. Chem. Soc.* **2021**, *143*, 2156−2163.
(26) Gauthier, N.; Argouarch, G.; Paul, F.; Humphrey, M. G.; Toupet, L.; Ababou-Girard, S.; Sabbah, H.; Hapiot, P.; Fabre, B. Silicon Surface-Bound Redox-Active Conjugated Wires Derived From Mono-and Dinuclear Iron (II) and Ruthenium (II) Oligo (phenyleneethynylene) Complexes. *Adv. Mater.* **2008**, *20*, 1952−1956.
(27) Ciampi, S.; Eggers, P. K.; Le Saux, G.; James, M.; Harper, J. B.; Gooding, J. J. Silicon (100) electrodes resistant to oxidation in aqueous solutions: an unexpected benefit of surface acetylene moieties. *Langmuir* **2009**, *25*, 2530−2539.
(28) Ciampi, S.; James, M.; Darwish, N.; Luais, E.; Guan, B.; Harper, J. B.; Gooding, J. J. Oxidative acetylenic coupling reactions as a surface chemistry tool. *Phys. Chem. Chem. Phys.* **2011**, *13*, 15624−15632.
(29) Ciampi, S.; James, M.; Le Saux, G.; Gaus, K.; Justin Gooding, J. Electrochemical "switching" of Si (100) modular assemblies. *J. Am. Chem. Soc.* **2012**, *134*, 844−847.
(30) O'Leary, L. E.; Rose, M. J.; Ding, T. X.; Johansson, E.; Brunschwig, B. S.; Lewis, N. S. Heck coupling of olefins to mixed methyl/thienyl monolayers on Si (111) surfaces. *J. Am. Chem. Soc.* **2013**, *135*, 10081−10090.
(31) Fabre, B.; Pujari, S. P.; Scheres, L.; Zuilhof, H. Micropatterned ferrocenyl monolayers covalently bound to hydrogen-terminated

silicon surfaces: effects of pattern size on the cyclic voltammetry and capacitance characteristics. *Langmuir* **2014**, *30*, 7235−7243.
(32) Yang, Y.; Ciampi, S.; Choudhury, M. H.; Gooding, J. J. Light activated electrochemistry: light intensity and pH dependence on electrochemical performance of anthraquinone derivatized silicon. *J. Phys. Chem. C* **2016**, *120*, 2874−2882.
(33) Zhang, L.; Vogel, Y. B.; Noble, B. B.; Gonçales, V. R.; Darwish, N.; Brun, A. L.; Gooding, J. J.; Wallace, G. G.; Coote, M. L.; Ciampi, S. TEMPO monolayers on Si (100) electrodes: electrostatic effects by the electrolyte and semiconductor space-charge on the electroactivity of a persistent radical. *J. Am. Chem. Soc.* **2016**, *138*, 9611−9619.
(34) Gonçales, V. R.; Lian, J.; Gautam, S.; Hagness, D.; Yang, Y.; Tilley, R. D.; Ciampi, S.; Gooding, J. J. Heterojunctions based on amorphous silicon: a versatile surface engineering strategy to tune peak position of redox monolayers on photoelectrodes. *J. Phys. Chem. C* **2020**, *124*, 836−844.
(35) Mukhopadhyay, A.; Bernard, B.; Liu, K.; Paulino, V.; Liu, C.; Donley, C.; Olivier, J.-H. Molecular Strategies to Modulate the Electrochemical Properties of P-Type Si (111) Surfaces Covalently Functionalized with Ferrocene and Naphthalene Diimide. *J. Phys. Chem. B* **2019**, *123*, 11026−11041.
(36) Mukhopadhyay, A.; Paulino, V.; Liu, K.; Donley, C. L.; Bernard, B.; Shomar, A.; Liu, C.; Olivier, J.-H. Leveraging the Assembly of a Rylene Dye to Tune the Semiconducting Properties of Functionalized n-Type, Hybrid Si Interfaces. *ACS Appl. Mater. Interfaces* **2021**, *13*, 4665.
(37) Hauquier, F.; Ghilane, J.; Fabre, B.; Hapiot, P. Conducting ferrocene monolayers on nonconducting surfaces. *J. Am. Chem. Soc.* **2008**, *130*, 2748−2749.
(38) Figueira-Duarte, T. M.; Müllen, K. Pyrene-based materials for organic electronics. *Chem. Rev.* **2011**, *111*, 7260−7314.
(39) Mei, J.; Diao, Y.; Appleton, A. L.; Fang, L.; Bao, Z. Integrated materials design of organic semiconductors for field-effect transistors. *J. Am. Chem. Soc.* **2013**, *135*, 6724−6746.
(40) Jiang, W.; Li, Y.; Wang, Z. Tailor-made rylene arrays for high performance n-channel semiconductors. *Acc. Chem. Res.* **2014**, *47*, 3135−3147.
(41) Al Kobaisi, M.; Bhosale, S. V.; Latham, K.; Raynor, A. M.; Bhosale, S. V. Functional naphthalene diimides: synthesis, properties, and applications. *Chem. Rev.* **2016**, *116*, 11685−11796.
(42) Nowak-Król, A.; Shoyama, K.; Stolte, M.; Würthner, F. Naphthalene and perylene diimides−better alternatives to fullerenes for organic electronics? *Chem. Commun.* **2018**, *54*, 13763−13772.
(43) Liang, N.; Meng, D.; Wang, Z. Giant rylene imide-based electron acceptors for organic photovoltaics. *Acc. Chem. Res.* **2021**, *54*, 961−975.
(44) Würthner, F. Perylene bisimide dyes as versatile building blocks for functional supramolecular architectures. *Chem. Commun.* **2004**, *14*, 1564−1579.
(45) Huang, C.; Barlow, S.; Marder, S. R. Perylene-3, 4, 9, 10-tetracarboxylic acid diimides: synthesis, physical properties, and use in organic electronics. *J. Org. Chem.* **2011**, *76*, 2386−2407.
(46) Würthner, F.; Saha-Möller, C. R.; Fimmel, B.; Ogi, S.; Leowanawat, P.; Schmidt, D. Perylene bisimide dye assemblies as archetype functional supramolecular materials. *Chem. Rev.* **2016**, *116*, 962−1052.
(47) Olivier, J.-H.; Park, J.; Deria, P.; Rawson, J.; Bai, Y.; Kumbhar, A. S.; Therien, M. J. Unambiguous Diagnosis of Photoinduced Charge Carrier Signatures in a Stoichiometrically Controlled Semiconducting Polymer-Wrapped Carbon Nanotube Assembly. *Angew. Chem., Int. Ed.* **2015**, *54*, 8133−8138.
(48) Krieg, E.; Niazov-Elkan, A.; Cohen, E.; Tsarfati, Y.; Rybtchinski, B. Noncovalent aqua materials based on perylene diimides. *Acc. Chem. Res.* **2019**, *52*, 2634−2646.
(49) Leira-Iglesias, J.; Sorrenti, A.; Sato, A.; Dunne, P. A.; Hermans, T. M. Supramolecular pathway selection of perylenediimides mediated by chemical fuels. *Chem. Commun.* **2016**, *52*, 9009−9012.
(50) Leira-Iglesias, J.; Tassoni, A.; Adachi, T.; Stich, M.; Hermans, T. M. Oscillations, travelling fronts and patterns in a supramolecular system. *Nat. Nanotechnol.* **2018**, *13*, 1021−1027.
(51) Liu, K.; Levy, A.; Liu, C.; Olivier, J.-H. Tuning Structure−Function Properties of π-Conjugated Superstructures by Redox-Assisted Self-Assembly. *Chem. Mater.* **2018**, *30*, 2143−2150.
(52) Liu, K.; Mukhopadhyay, A.; Ashcraft, A.; Liu, C.; Levy, A.; Blackwelder, P.; Olivier, J.-H. Reconfiguration of π-conjugated superstructures enabled by redox-assisted assembly. *Chem. Commun.* **2019**, *55*, 5603−5606.
(53) Ashcraft, A.; Liu, K.; Mukhopadhyay, A.; Paulino, V.; Liu, C.; Bernard, B.; Husainy, D.; Phan, T.; Olivier, J. H. A molecular strategy to lock-in the conformation of a perylene bisimide-derived supramolecular polymer. *Angew. Chem., Int. Ed.* **2020**, *59*, 7487−7493.
(54) Coropceanu, V.; Cornil, J.; da Silva Filho, D. A.; Olivier, Y.; Silbey, R.; Brédas, J.-L. Charge transport in organic semiconductors. *Chem. Rev.* **2007**, *107*, 926−952.
(55) Hestand, N. J.; Spano, F. C. Molecular aggregate photophysics beyond the Kasha model: novel design principles for organic materials. *Acc. Chem. Res.* **2017**, *50*, 341−350.
(56) Hestand, N. J.; Spano, F. C. Expanded theory of H-and J-molecular aggregates: the effects of vibronic coupling and intermolecular charge transfer. *Chem. Rev.* **2018**, *118*, 7069−7163.
(57) Shirman, E.; Ustinov, A.; Ben-Shitrit, N.; Weissman, H.; Iron, M. A.; Cohen, R.; Rybtchinski, B. Stable aromatic dianion in water. *J. Phys. Chem. B* **2008**, *112*, 8855−8858.
(58) Schlosser, F.; Moos, M.; Lambert, C.; Würthner, F. Redox-switchable Intramolecular $\pi-\pi$-Stacking of Perylene Bisimide Dyes in a Cyclophane. *Adv. Mater.* **2013**, *25*, 410−414.
(59) Higashi, T.; Sagara, T. Diphenyl viologen on an HOPG electrode surface: less sharp redox wave than dibenzyl viologen. *Langmuir* **2013**, *29*, 11516−11524.
(60) Avestro, A.-J.; Gardner, D. M.; Vermeulen, N. A.; Wilson, E. A.; Schneebeli, S. T.; Whalley, A. C.; Belowich, M. E.; Carmieli, R.; Wasielewski, M. R.; Stoddart, J. F. Gated electron sharing within dynamic naphthalene diimide-based oligorotaxanes. *Angew. Chem., Int. Ed.* **2014**, *53*, 4442−4449.
(61) Espinoza, E. M.; Clark, J. A.; Soliman, J.; Derr, J. B.; Morales, M.; Vullev, V. I. Practical aspects of cyclic voltammetry: How to estimate reduction potentials when irreversibility prevails. *J. Electrochem. Soc.* **2019**, *166*, H3175.
(62) Liu, K.; Paulino, V.; Mukhopadhyay, A.; Bernard, B.; Kumbhar, A.; Liu, C.; Olivier, J.-H. How to reprogram the excitonic properties and solid-state morphologies of π-conjugated supramolecular polymers. *Phys. Chem. Chem. Phys.* **2021**, *23*, 2703−2714.
(63) Ababou-Girard, S.; Cordier, S.; Fabre, B.; Molard, Y.; Perrin, C. Assembly of hexamolybdenum metallic clusters on silicon surfaces. *ChemPhysChem* **2007**, *8*, 2086−2090.
(64) Fabre, B.; Cordier, S.; Molard, Y.; Perrin, C.; Ababou-Girard, S.; Godet, C. Electrochemical and charge transport behavior of molybdenum-based metallic cluster layers immobilized on modified n-and p-type Si (111) surfaces. *J. Phys. Chem. C* **2009**, *113*, 17437−17446.
(65) Fabre, B.; Bassani, D. M.; Liang, C.-K.; Ray, D.; Hui, F.; Hapiot, P. Anthracene and anthracene: C60 adduct-terminated monolayers covalently bound to hydrogen-terminated silicon surfaces. *J. Phys. Chem. C* **2011**, *115*, 14786−14796.
(66) Jalkh, J.; Thiery, S.; Bergamini, J.-F.; Hapiot, P.; Poriel, C.; Leroux, Y. R. Influence of Fluorene and Spirobifluorene Regioisomerism on the Structure, Organization, and Permeation Properties of Monolayers. *J. Phys. Chem. C* **2017**, *121*, 14228−14237.
(67) Arramel; Yin, X.; Wang, Q.; Zheng, Y. J.; Song, Z.; Bin Hassan, M. H.; Qi, D.; Wu, J.; Rusydi, A.; Wee, A. T. Molecular Alignment and Electronic Structure of N, N′-Dibutyl-3, 4, 9, 10-Perylene-Tetracarboxylic-Diimide Molecules on MoS2 Surfaces. *ACS Appl. Mater. Interfaces* **2017**, *9*, 5566−5573.
(68) Kato, D.; Sakai, H.; Araki, Y.; Wada, T.; Tkachenko, N. V.; Hasobe, T. Concentration-dependent photophysical switching in

https://doi.org/10.1021/acsanm.1c01473
ACS Appl. Nano Mater. 2021, 4, 8813−8822

mixed self-assembled monolayers of pentacene and perylenediimide on gold nanoclusters. *Phys. Chem. Chem. Phys.* **2018**, *20*, 8695−8706.
(69) Lee, S. K.; Zu, Y.; Herrmann, A.; Geerts, Y.; Müllen, K.; Bard, A. J. Electrochemistry, spectroscopy and electrogenerated chemiluminescence of perylene, terrylene, and quaterrylene diimides in aprotic solution. *J. Am. Chem. Soc.* **1999**, *121*, 3513−3520.
(70) Shan, B.; Nayak, A.; Brennaman, M. K.; Liu, M.; Marquard, S. L.; Eberhart, M. S.; Meyer, T. J. Controlling Vertical and Lateral Electron Migration Using a Bifunctional Chromophore Assembly in Dye-Sensitized Photoelectrosynthesis Cells. *J. Am. Chem. Soc.* **2018**, *140*, 6493−6500.

https://doi.org/10.1021/acsanm.1c01473
ACS Appl. Nano Mater. 2021, 4, 8813−8822